Biophysical Journal
Article

Biophysical Society

Iomeprol X-ray contrast media alter conformation and affinity of the ATP binding pocket of actin

Elek Telek,[1] Gábor Hild,[1] Veronika Takács-Kollár,[1] Balázs Zoltán Zsidó,[2] Csaba Hetényi,[2,3] Kinga Ujfalusi-Pozsonyi,[1] Zétény Csonka,[1] Bálint Bécsi,[4] András Lukács,[1] Sándor Kunsági-Máté,[5,6] Gabriella Hild,[7] and Zoltán Ujfalusi[1,*]

[1]Department of Biophysics, Medical School, University of Pécs, Szigeti str. 12, 7624 Pécs, Hungary; [2]Pharmacoinformatics Unit, Department of Pharmacology and Pharmacotherapy, Medical School, University of Pécs, Szigeti str 12, 7624 Pécs, Hungary; [3]National Laboratory for Drug Research and Development, Budapest, Hungary; [4]Department of Medical Chemistry, Faculty of Medicine, University of Debrecen, Egyetem square 1, 4043 Debrecen, Hungary; [5]Department of Organic and Medicinal Chemistry, Faculty of Pharmacy, University of Pécs, Honvéd str 1, 7624 Pécs, Hungary; [6]János Szentágothai Research Center, Ifjúság útja 20, 7624 Pécs, Hungary; and [7]Languages for Biomedical Purposes and Communication, Medical School, University of Pécs, Szigeti str. 12, 7624 Pécs, Hungary

ABSTRACT Contrast materials are widely used in various X-ray/CT and MRI diagnostic procedures. When administered in high volumes, contrast agents can strain kidney function and lead to acute renal failure. Contrast materials may damage the plasma membrane and penetrate into tissue cells. Some iodine-based contrast agents have been reported to distort the shape of red blood cells, implying a rearrangement of the actin cytoskeletal network. As actin plays a crucial role in numerous cellular processes, the effects of iodine-based contrast media on actin require clarification. We characterized the effect of iomeprol on the structure and function of actin using calorimetry, co-sedimentation, fluorescence spectroscopy, and molecular docking. Our results revealed that iomeprol disassembles the F-actin network by interacting with G-actin, suggesting a direct influence on its structural and functional properties. In line with this, polymerization and dilution-induced depolymerization assays, as well as critical concentration measurements, showed pronounced effects on actin dynamics. Iomeprol alters the conformation of G-actin, particularly the ATP-binding pocket—which becomes more open—and significantly (∼3-fold) decreases ATP affinity. Molecular docking supported these findings, indicating that iomeprol interacts with the ATP-binding cleft of G-actin. An additional interaction site was identified in the SD1/3 cleft—a known binding site for Wiskott-Aldrich syndrome protein and profilin—suggesting that iomeprol may also influence the association and dissociation dynamics of actin-binding proteins. Overall, our findings indicate that iomeprol can influence the structural and functional properties of actin, raising the possibility that such alterations may contribute to changes in actin organization and, consequently, to actin-dependent cellular processes.

SIGNIFICANCE Contrast agents are indispensable in diagnostic imaging, yet their molecular effects remain poorly understood. We show that the iodine-based agent iomeprol, used in X-ray and CT procedures, modifies actin, a key cytoskeletal protein, by altering its structure and reducing ATP binding. Because actin is fundamental to a wide range of cellular processes, even modest perturbations may influence cell integrity and, in susceptible tissues, contribute to functional impairment. Our findings highlight an unrecognized molecular interaction through which contrast agents can modulate actin behavior, offering a mechanistic link between basic biochemical effects and clinically observed cellular stress. This work broadens understanding of how contrast agents affect cells and provides a foundation for safer diagnostic strategies and the development of improved imaging materials.

INTRODUCTION

A general problem that images produced from certain tissues using medical imaging equipment is that they lack good contrast. In such cases, contrast materials (CMs) are valuable

Submitted December 9, 2025, and accepted for publication May 11, 2026.

*Correspondence: zoltan.ujfalusi@aok.pte.hu

Editor: James Gumbart.

https://doi.org/10.1016/j.bpj.2026.05.015

tools for enhancing the density and intensity of vessels, body parts, organs, or tissues.

There was already a great need for CMs in the late 1800s, when it was discovered that elements with higher atomic numbers exhibit greater absorption/attenuation of X-rays. The first contrast agents used experimentally were bismuth, lead, and barium salts.[1] However, for human applications, agents with significantly lower toxicity must be identified. In the early 1920s, it was accidentally discovered that the iodine-containing compounds used to treat syphilis had excellent X-ray absorption properties, which could be harnessed for human diagnostics.[2]

Currently, there are numerous CM options for improved visualization of specific areas in X-ray/CT and MRI diagnostics, interventional radiology, cardiac catheterization, and other procedures.[3–8] In many cases, CM is used in high volumes, placing a heavy burden on kidney function. Even a few years ago, contrast agent administration was identified as the third leading cause of hospital-acquired acute kidney injury (after surgery and hypotension), accounting for 11% of all cases of acute kidney injury. Despite recommendations and cautious use of CM, approximately 5% of hospitalized patients with normal renal function develop acute renal failure after contrast administration.[9]

The precise pathophysiology of contrast-induced nephropathy is not fully understood, although many aspects have been clarified, such as cytotoxicity, intrarenal vasoconstriction, and the appearance of reactive oxygen species.[10] While the general physiological effects and impacts on red blood cells have been described in several publications, the underlying molecular mechanisms remain poorly understood. CM drug molecules damage the plasma membrane of cells,[11] penetrate the cells of tissues, and may accumulate there due to their limited clearance.[12] Iodinated contrast agents are also known to reach exceptionally high local concentrations *in vivo*. Pharmacokinetic studies indicate that, when calculated over the total blood volume, the systemic plasma concentration of iomeprol after administration typically falls in the 5–40 mM range.[13,14] Locally, such as immediately after intra-arterial injection into the coronary circulation, the transient peak concentration can be substantially higher than the systemic value, although this does not reflect the molarity averaged over the entire blood volume. Several studies have demonstrated that contrast media can accumulate within renal tubular fluid and inside tubular epithelial cells, where slow clearance, osmotic effects, and endosomal-lysosomal sequestration may lead to concentrations in the tens to hundreds of millimolar range.[15–18] Beyond the kidney, various interventional procedures can transiently expose local tissues to markedly elevated intra-arterial contrast concentrations, imposing substantial chemical and osmotic stress on the affected cells—for example within the coronary circulation,[19] during first-pass cerebral perfusion,[20] or in the hepatic parenchyma.[21] These observations provide a physiological rationale for investigating the molecular effects of contrast agents not only at micromolar but also at millimolar concentrations *in vitro*. Some iodine-containing contrast agents alter the morphology of red blood cells,[22] an effect that is thought to be triggered by the rearrangement of the actin network adjacent to the cell membrane.[23]

Actin can be found in cells in two forms: monomeric or globular (G-actin), and polymeric or filamentous (F-actin). G-actin contains four subdomains (SD 1–4) featuring a deep ATP-binding cleft and an SD1/3 cleft (Figure 1), which is a prominent groove between subdomains 1 and 3 that interacts with actin -binding proteins.[24] The SD1/3 binding pocket plays a critical role in actin function by enabling interactions with actin-binding proteins, such as the WH2 domain of Wiskott-Aldrich syndrome protein (WASP) and profilin. The WH2 domain of WASP binds to G-actin and promotes the interaction with the Arp2/3 complex, stimulating the formation of branched actin cytoskeletal networks.[25] In addition, profilin can bind to the SD1/3 cleft and participates in regulating actin polymerization dynamics.[26]

Filaments are composed of monomers that are attached to each other by noncovalent bonds. Actin filaments play an essential role in several processes in eukaryotic cells, including the maintenance of cell shape, cell junctions, motility, polarity, division, intracellular transport, and signal transduction.[27–33] Most of these processes are mediated by actin-binding proteins, which cause actin filament rearrangement in different ways.

We have previously published our results on the effects of iomeprol, iobitridol, and iodixanol X-ray/CT contrast agents on human blood components.[34,35]

Recently, we have focused on comprehensively investigating the effects of contrast agents on the structure and functional dynamics of actin. Our goal was to better understand the molecular mechanisms underlying irreversible cellular damage associated with CM exposure.

MATERIALS AND METHODS

Protein purification

Actin was purified from rabbit (*Oryctolagus cuniculus)* skeletal muscle acetone powder according to a method modified from that described by Spudich and Watt.[36] Finally, actin was stored in buffer "A" (4 mM Tris-HCl, 0.1 mM $CaCl_2$, 0.2 mM ATP, 0.5 mM β-mercaptoethanol [MEA], 0.005% NaN_3, pH 7.5). To measure F-actin, polymerization was performed for 1 h using 100 mM KCl and 2 mM $MgCl_2$ prior to the experiments.

ATP depletion of actin

For ATP-related fluorescence spectroscopic measurements, ATP was eliminated from G-actin. Prior to ATP depletion,

the Eppendorf centrifuge was chilled to 4°C. G-actin was diluted to 50 μM in 1.2 mL of ATP-free buffer "A" (4 mM Tris-HCl, 0.1 mM $CaCl_2$, 0.5 mM β-mercaptoethanol, 0.005% NaN_3, pH 7.5) in an Eppendorf tube. To eliminate the bound ATP from G-actin, a Dowex (Sigma-aldrich) ion exchanger resin was used. First, 1 mL Dowex was diluted with 1 mL ATP-free buffer "A" to obtain 50% (w/v) resin. Then, 180 μL of Dowex mixture was added to 50 μM of diluted G-actin by inverting the tube 2–4 times. The mixture was centrifuged immediately for 3 min (13,000 rcf at 4°C). In this step, unbound ATP was removed from the buffer. The supernatant was pipetted into another Eppendorf tube and mixed again with 180 μL of Dowex mixture followed by another centrifugation for 2 min (13,000 rcf at 4°C). In this second step, the G-actin bound ATP was eliminated. Finally, ATP-free G-actin supernatant was pipetted into a new Eppendorf tube and used immediately for mant-ATP fluorescence-based measurements.

Treatment with contrast media

G-actin and F-actin samples were treated with Iomeron CM and incubated for 30 min prior to the measurements. Iomeron (300 mg I/mL) solution contains 61.24% (m/v) iomeprol (N, N0-bis(2, 3-dihydroxypropyl)-5[(hydroxyacetyl)methylamino]-2, 4, 6-triiodo-1, 3-benzenedicarboxamide) as an active material.

Isothermal titration calorimetry

Isothermal titration calorimetry (ITC) experiments were carried out with MicroCal ITC200 instrument. The measurements were performed under identical buffer conditions (2 mM Tris-HCl, 0.1 mM $CaCl_2$, 0.2 mM ATP, 0.005% NaN_3, pH 7.5). G-actin (2.5 μM) was loaded into the sample cell of the calorimeter while the reference cell was filled with buffer. In the assay, iomeprol (50 μM) was applied to the syringe, and 2-μL aliquots (19 times) were injected into the cell at a stirring rate of 300 rpm at 25°C. The reference power was set to 5 μcal/s. The titration data were analyzed with Microcal Origin 7 software (Malvern Instruments, Malvern, UK) using one set of site model to obtain the binding parameters of the G-actin-iomeprol interaction. Data were plotted using the Origin 2022b software (OriginLab Corporation, Northampton, USA).

Differential scanning calorimetry

The thermodynamic properties of G-, and F-actin samples (46 μM) were studied in the absence and presence of iomeprol (40, 80 mM) with a SETARAM micro DSC-III calorimeter. The measurements were carried out at heating rates of 0.3 K/min^{-1} between 20°C and 100°C. The appropriate mixture of actin and iomeprol as well as the reference (buffer "A") was 850 μL. The samples and reference were pipetted in conventional Hastelloy batch vessels (V_{max} = ~1 mL) for the measurements. Then, the sample and reference vessels were balanced with a precision of ±0.05 mg; therefore, correction was not necessary for the heat capacity of the vessels. The second heat denaturation step was used for baseline correction of the heat flow data. Data were analyzed with Origin 2022b, and the melting temperature (T_m) and change in enthalpy (ΔH) were determined to characterize the thermodynamic properties of actin. All necessary control experiments were performed for buffer and contrast agent effects with no significant results (data not shown).

Co-sedimentation assay

In order to study the F:G-actin ratio, a co-sedimentation assay was performed. Actin (10 μM; 200 μL) was polymerized under high-salt conditions (2 mM $MgCl_2$, 100 mM KCl) in the presence of increasing iomeprol concentrations (2.5–80 mM) at room temperature for 2 h. Then, it was centrifuged at 386,000 × g, 4°C for 30 min. G-actin samples were obtained by gently pipetting 150 μL of the supernatant and, after, added to 75 μL of Laemmli solution with β-mercaptoethanol (BME). 200 μL buffer "A" and 100 μL Laemmli solution (with BME) were added to the F-actin pellets. Then, the G- and F-actin mixtures were subjected to polyacrylamide gel electrophoresis (PAGE) separately using a 12% gel. After PAGE, the gel was stained with brilliant blue dye for 1 h. Then, unbound dye was removed from the gel using destaining solution. Finally, densitometric analysis was carried out to analyze the amount of G- and F-actin in the samples. Data were visualized using Origin 2022b software.

Fluorescence emission-based spectral shift measurements

Fluorescence emission of 1 μM mant-ATP was measured by HORIBA Jobin Yvon Fluorolog 3.22 spectrofluorometer. The measurements were performed in buffer "A" without ATP (4 mM Tris-HCl, 0.1 mM $CaCl_2$, 0.5 mM MEA, 0.005% NaN_3, pH 7.5). Mant-ATP was excited at 365 nm in order to exclude the excitation of iomeprol. The emission spectra were recorded between 400 and 600 nm using 10 nm excitation and 10 nm emission slits at 20°C. For control measurements, fluorescence emission of mant-ATP was measured in the absence and presence of 40 and 80 mM iomeprol. Subsequently, we performed fluorescence emission of mant-ATP at increasing concentration of ATP-depleted G-actin in the absence and presence of iomeprol (40, 80 mM). To evaluate the fluorescence spectra of mant-ATP upon G-actin addition, we used Origin 2022b to plot the maximum wavelength (λ_{max}) of mant-ATP fluorescence emission, and a quadratic binding equation[1] was fitted to obtain the dissociation equilibrium constant.

$$\frac{r - rA}{rAP - rA} = \frac{A_o + P_o + K_D - \sqrt{(A_o + P_o + K_D)^2 - 4 * A_o * P_o}}{2}, \quad (1)$$

where A_o and P_o are the total mant-ATP and G-actin concentrations, respectively, rA is the maximum wavelength of mant-ATP, rAP is the maximum wavelength of mant-ATP at a saturating amount of G-actin and K_D is the dissociation equilibrium constant of the mant-ATP-G-actin complex.

Molecular docking

Ligand preparation

The 3D structure of 1-N,3-N-bis(2,3-dihydroxypropyl)-5-(2-hydroxy-N-methylacetamido)-2,4,6-triiodobenzene-1,3-dicarboxamide (iomeprol) was built in Maestro[37] optimized by a built-in energy minimization with the software. For docking, Gasteiger-Marsili partial charges[38] were added in AutoDockTools,[39] and the ligand was saved in pdbqt format.

Target preparation

The atomic coordinates of G-actin from rabbits (*Oryctolagus cuniculus*) in the ligand-free (apo) form were obtained from the Protein Data Bank (PDB) under the accession code PDB: 3hbt.[40] Adenosine triphosphate (ATP) was then removed. Missing amino acid residues or atoms were built with SWISS-MODEL.[41] Hydrogens and Gasteiger-Marsili partial charges were added to G-actin using AutoDockTools.

Wrap'n'Shake protocol

The Wrapper part of the Wrap'n'Shake[42] method was used to build a monomolecular layer of iomeprol molecules on the surface of G-actin. The grid box was placed at the center of the G-actin, and its size was increased to cover the entire surface of the protein. The settings were set according to the original publication[42] and a recent study of our group.[43] The maximal number of docking cycles was set to 30, and 100 docking calculations were performed in each cycle until the energetic exit criterion ($E_{inter} > +1$ kcal/mol) was reached in the 15th cycle. The docked binding modes were clustered into ranks. A lower rank corresponds to a more favorable binding energy (E_{inter}). After clustering a total of 323 iomeprol copies were placed on the G-actin, and 134 remained after trimming (keeping only those that are within 3.5 Å of the target).

Fluorescence labeling of actin

Actin was labeled with N-(1-pyrene)iodoacetamide (Molecular Probes, Thermo Fisher Scientific, USA) as previously described to determine the critical concentration and to monitor actin polymerization/depolymerization kinetics in the presence of iomeprol.[44] Shortly, monomeric actin was polymerized in β-mercaptoethanol-free buffer "A" for 1 h at room temperature. The pyrene-iodoacetamide was dissolved in DMSO to a final concentration of 5 mg/mL. The filamentous actin was incubated with a 1.1-fold molar excess of fluorophore for 18 h at room temperature. The sample was ultracentrifuged at 328,000 × *g* for 45 min at 4°C in order to separate labeled actin from free fluorophore. The actin concentration was determined using a Shimadzu spectrophotometer and an extinction coefficient of 0.63 mg^{-1} mL cm^{-1} at 290 nm. The actin-bound pyrene-iodoacetamide concentration was calculated by the absorption coefficient of 45,000 $M^{-1}cm^{-1}$ at 344 nm. The labeling ratio was 75%–95%.

Actin polymerization assay

N-(1-pyrene)iodoacetamide-labeled actin was applied to monitor the actin polymerization kinetics. The actin polymerization assay was carried out with a Cary Eclipse Fluorescence Spectrophotometer (Agilent Technologies, United States). The measurements were performed by using 2.5 μM unlabeled actin, containing 5% labeled with pyrene. The excitation wavelength was 365 nm, while the emission was detected at 407 nm. The Mg^{2+}-actin polymerization was initiated by the addition of 2 mM $MgCl_2$ and 100 mM KCl in the absence or presence of iomeprol (5–80 mM). For quantitative analysis, the polymerization rate was determined from the slope of the linear region of the pyrene fluorescence trace under each condition. The relative polymerization rate was calculated as the ratio between the polymerization rates measured in the presence and absence of the contrast agent.

Dilution-induced actin depolymerization assay

The kinetics of actin disassembly can be followed using N-(1-pyrene)iodoacetamide-labeled actin, with excitation at 365 nm and emission detected at 407 nm. The depolymerization assay was carried out with a Cary Eclipse Fluorescence Spectrophotometer. Mg^{2+}-G-actin labeled with pyrene (1 μM, 50% labeled) was polymerized in the presence of 2 mM $MgCl_2$ and 100 mM KCl. The pyrene-labeled F-actin was diluted to 20 nM to trigger the net disassembly of the actin filaments. As the 20 nM is below the critical concentration of actin ($c_{actin\ cc} \sim 100$ nM) the actin filaments

are depolymerized.[45] The depolymerization rate was determined from the double-exponential fit (Equation 2) applied to the primer depolymerization curves,

$$y = A_1 \cdot e^{-\frac{x}{t_1}} + A_2 \cdot e^{-\frac{x}{t_2}} + y_0, \quad (2)$$

where A_1 and A_2 denote the amplitudes of the fast and slow exponential components, respectively; t_1 and t_2 are the corresponding time constants; e is the base of the natural logarithm; and y_0 represents the baseline offset. We plotted the values of the t_1 time constant, which corresponds to the faster exponential component and provides a reliable measure of the initial, rapid phase of actin filament depolymerization—that is, the kinetically dominant portion of the decay process. The relative polymerization rate was calculated as the ratio of polymerization rates obtained in the presence and absence of iomeprol.

Critical concentration measurements

Pyrene-labeled actin was excited at 365 nm, and emission was recorded at 407 nm. The fluorescence of monomeric pyrene-G-actin remained low and nearly constant across subcritical concentrations. Because pyrene fluorescence increases upon incorporation into F-actin, the emission intensity reports the fraction of polymerized actin. Fluorescence intensity was plotted against total actin concentration, and two linear regressions were fitted: one to the low-intensity region corresponding to unpolymerized actin (Equation 2) and one to the increasing intensities associated with filament formation (Equation 3). Control measurements yielded values within the expected 100–300 nM range for Mg^{2+}-actin *in vitro*.[46]

$$Y_1 = a_1 + b_1X \quad (3)$$

$$Y_2 = a_2 + b_2X \quad (4)$$

Here, Y denotes the measured fluorescence emission intensity, X is the total actin concentration, a is the intercept of the fitted line, and b represent their respective slopes. The intersection of Equations 3 and 4 defines the critical concentration.

RESULTS

Iomeprol binds G-actin and influence the conformational stability of monomeric and filamentous forms

To investigate the interaction between G-actin and iomeprol molecule, we performed ITC measurements. ITC can measure the affinity of proteins and small molecules as well as their thermodynamic parameters characterizing the interaction.[47,48] The measurements revealed that iomeprol binds to G-actin with a K_A of 1.05 ± 0.4 μM^{-1} affinity, and the calculated dissociation constant resulted in a K_D of 0.95 ± 2.46 μM, suggesting a strong affinity. The stoichiometry of G-actin:iomeprol was 1:1 (1.02 ± 0.154 sites), revealing that one iomeprol molecule interacts with one G-actin molecule. In addition, the thermodynamic parameters of the interaction were the following: ΔH = −4.987 ± 0.995 kcal/mol and the ΔS = 0.0108 kcal/mol/deg (Figure 2; Table 1). The high exothermic change of the interaction can be attributed to the structural change in actin under contrast agent administration conditions.

To study the effect of iomeprol on actin conformation, we performed differential scanning calorimetry (DSC) measurements,[49] which is a powerful method for the thermodynamic characterization of proteins.[50–53] Thermal unfolding of G-actin (black) showed a melting temperature (T_m) of 58.2°C ± 0.28°C, and the change in enthalpy (ΔH) was 687.5 ± 147.19 KJ/mol. Upon the addition of 40 mM iomeprol (red), the T_m of G-actin decreased to 57.2°C ± 0.56°C, and ΔH (637.2 ± 112.65 KJ/mol) declined. When 80 mM of iomeprol (blue) was added, the thermodynamic parameters of G-actin further decreased. T_m showed a drop to 56.3°C ± 0.63°C, which is a 1.9°C decline compared with the control. In addition, ΔH (563.3 ± 49.76 KJ/mol) also decreased considerably (Figure 3A; Table 2). Our findings indicate that the addition of increasing concentration of iomeprol changed the thermodynamic properties, which may destabilize the conformation and stability of G-actin.

In addition, we investigated the effect of iomeprol on F-actin filaments by DSC. Heat denaturation of F-actin (black) resulted in T_m = 67.1°C ± 0.14°C and ΔH = 744.7 ± 143.75 KJ/mol. The addition of 40 mM iomeprol

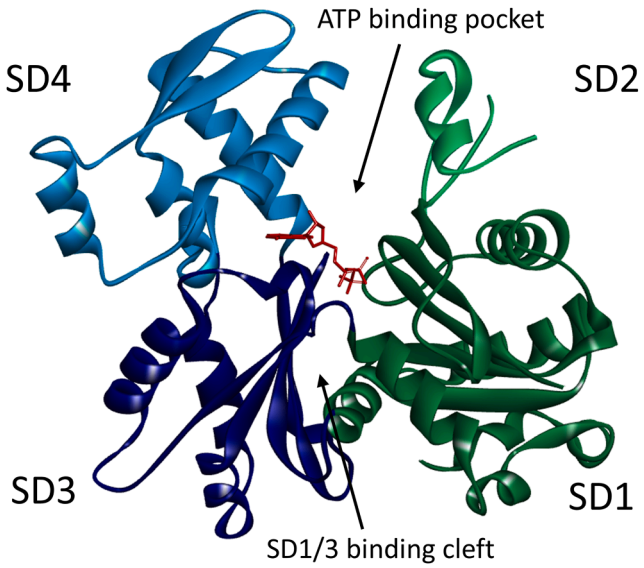

Figure 1. Structure of G-actin (PDB:3hbt). Subdomains are indicated as SD1–4. ATP binding cleft is shown in the pocket between SD2 and 4 with bound ATP (red). The SD1/3 cleft is also shown in the groove between SD1 and 3.

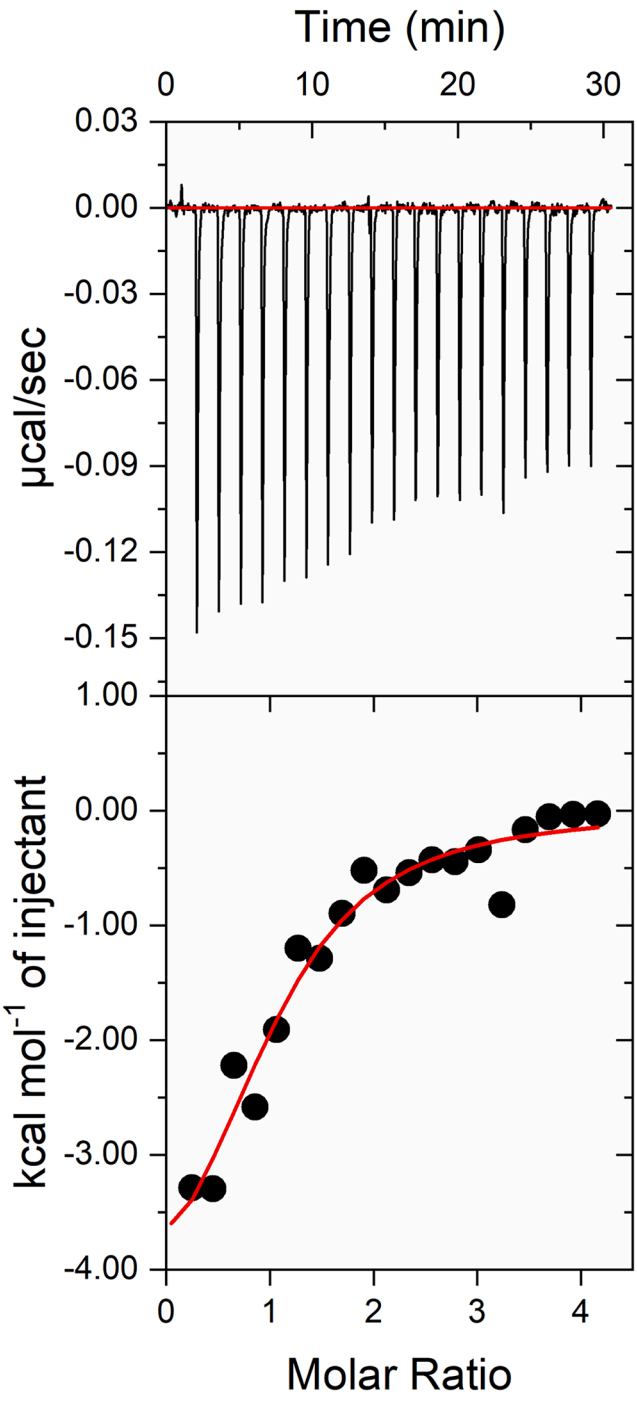

Figure 2. Iomeprol interacts with G-actin. The top panel shows the raw data of ITC measurement, where the area of each injection peak is equal to the total heat released from that injection. On the bottom panel, the integrated heat is plotted as a function of the molar ratio of iomeprol added to G-actin in the cell, which resulted in a complete binding isotherm for the interaction obtained. G-actin concentration was 2.5 µM, while 50 µM iomeprol was applied to the syringe, and 2-µL aliquots (19 times) were injected into the cell. The one set of the site model was used to fit the data to describe the number of binding sites, association constant, enthalpy, and entropy. Moreover, the equilibrium constant for dissociation was calculated using the reciprocal of the association constant.

to F-actin (red) revealed a considerable decrease in T_m = 59.7°C ± 0.77°C, as well as a marked decline in ΔH (ΔH = 637.9 ± 40.51 KJ/mol). Moreover, the addition of 80 mM iomeprol (blue) further decreased the thermodynamic properties of F-actin. T_m was 57.6°C ± 1.55°C, which is a significant decrease compared with the control F-actin (ΔT_m = 9.5°C), and ΔH was 606.2 ± 57.26 KJ/mol (Figure 3B; Table 2). These results revealed that iomeprol disrupts F-actin into G-actin monomers.

In order to corroborate the calorimetric findings of F-actin disassembly, we performed a high-speed co-sedimentation assay to investigate how the iodine-containing contrast agent influences the ratio of free G-actin to F-actin in dynamic equilibrium.[54] 10 µM F-actin was centrifuged in the presence of increasing concentration of iomeprol. The supernatant and pellet were separated and subjected to SDS-PAGE. We then analyzed the supernatant gel containing G-actin (Figure 4A). The intensity analysis showed that the amount of G-actin increased with rising iomeprol concentrations, indicating a shift toward the monomeric state. This concentration-dependent increase suggests that the presence of the contrast agent alters the F/G-actin equilibrium, although the underlying molecular mechanism remains unresolved (Figure 4B).

To further validate the destabilizing effect of iomeprol on F-actin suggested by the DSC and co-sedimentation assays, we monitored actin depolymerization kinetics in the presence of a broad concentration range of the contrast agent (Figures 5A and 5B). Remarkably, micromolar concentrations of iomeprol (1–10 µM) produced a depolymerization-accelerating effect comparable to that observed at millimolar concentrations. Both 5 µM and 10 µM iomeprol produced a pronounced increase in the depolymerization rate compared with the untreated control similarly to higher concentrations (40–80 mM). These findings indicate that iomeprol can promote filament disassembly already at low micromolar levels, consistent with the micromolar affinity observed by ITC, and suggest that distinct binding modes may differentially influence filament stability depending on concentration.

In addition, we examined whether iomeprol also affects the assembly phase of actin dynamics. Polymerization assays revealed a clear, concentration-dependent inhibition of filament growth (Figures 6A and 6B). At increasing concentrations, iomeprol progressively slowed actin polymerization, reaching an approximately 3-fold reduction in initial velocity at the highest concentration. These results complement the depolymerization data by demonstrating that iomeprol not only destabilizes pre-formed filaments but also interferes with the formation of new ones.

To assess whether iomeprol alters the thermodynamic equilibrium between G-, and F-actin, we determined the critical concentration in the presence of increasing concentrations of the contrast agent (Figure 7). The critical concentration of Mg^{2+}-actin under control conditions fell within

Table 1. Thermodynamic characterization of the interaction between G-actin and iomeprol

	Thermodynamic parameters by ITC				
	N (sites)	K_A *(μM^{-1})*	K_D *(μM)*	*ΔH (kcal/mol)*	*ΔS (kcal/mol/deg)*
G-actin + iomeprol	1.02 ± 0.154	1.05 ± 0.4	0.95 ± 2.46	−4.987 ± 0.995	0.0108

N, number of binding sites; K_A, association constant; K_D, dissociation constant; ΔH, binding enthalpy; ΔS, entropy.

the expected 100–300 nM range. Iomeprol induced only modest changes in this parameter: even at 80 mM, the critical concentration increased by approximately 2-fold. This relatively small shift indicates that iomeprol does not strongly perturb the equilibrium constant of polymerization, despite its clear effects on filament stability and polymerization kinetics. These findings suggest that iomeprol primarily influences the structural and dynamic properties of actin rather than fundamentally altering the thermodynamic balance between monomers and filaments.

Iomeprol modifies the conformation and affinity of the nucleotide binding pocket of actin

To investigate the effect of iomeprol on the nucleotide binding pocket of G-actin, we performed fluorescence emission spectral measurements. The fluorescence emission of 1 μM mant-ATP was monitored as a function of increasing concentration of ATP-free G-actin in the absence and presence of iomeprol (40, 80 mM). Mant-ATP is a hydrolysable, fluorescent ATP analog that has been extensively applied in fluorescence spectroscopic studies[55–59] as the intensity of mant-ATP increases upon binding.

Prior to the spectral measurements, we carried out control experiments without G-actin using 1 μM mant-ATP in the presence of 40 and 80 mM iomeprol. These measurements showed that the increasing concentration of iomeprol decreased the fluorescence emission of mant-ATP, which might be because the high iomeprol concentration (mM) somewhat quenched the mant-ATP (μM) fluorescence. However, more importantly, it did not shift the wavelength maxima of the fluorescence emission spectra, revealing that iomeprol itself does not affect the spectral shift of mant-ATP (Figures 8A and 8B).

Control experiments performed on G-actin in the absence of iomeprol showed an increase in the fluorescence emission of mant-ATP and a significant blueshift (16.3 nm) in the wavelength maxima from 446.6 to 430.3 nm (Figures 8C and 8F). These spectral changes reflect that mant-ATP nucleotides are less accessible to the solvent after binding and cause blue spectral shift, as they become buried in the native conformation of the nucleotide binding pocket of G-actin. In addition, treatment with 40 mM iomeprol revealed a less pronounced blueshift of approximately 7 nm from 446 to 439 nm (Figures 8D and F). Moreover, treatment with 80 mM iomeprol showed a slightly less significant blueshift (6.7 nm) from 446 to 438.7 nm (Figures 8E and 8F). This indicates that iomeprol may cause a change in the ATP binding pocket conformation of G-actin to a more flexible one, and mant-ATP is more surface exposed in the binding pocket.

To study the binding properties of mant-ATP to ATP-free G-actin in the absence and presence of 40 and 80 mM iomeprol a quadratic equation[1] was fitted to the wavelength maxima plot of mant-ATP fluorescence emission (Figure 5D). The data analysis resulted in a dissociation equilibrium constant (K_D) of 1.31 ± 0.62 μM for the G-actin control (Figure 8F, black). In the presence of 40 mM iomeprol, the fit to the data revealed a higher K_D of 4.26 ± 0.98 μM (Figure 8F, red). When 80 mM iomeprol was applied, there was a similarly high K_D of 4.55 ± 1.90 μM (Figure 8F, blue).

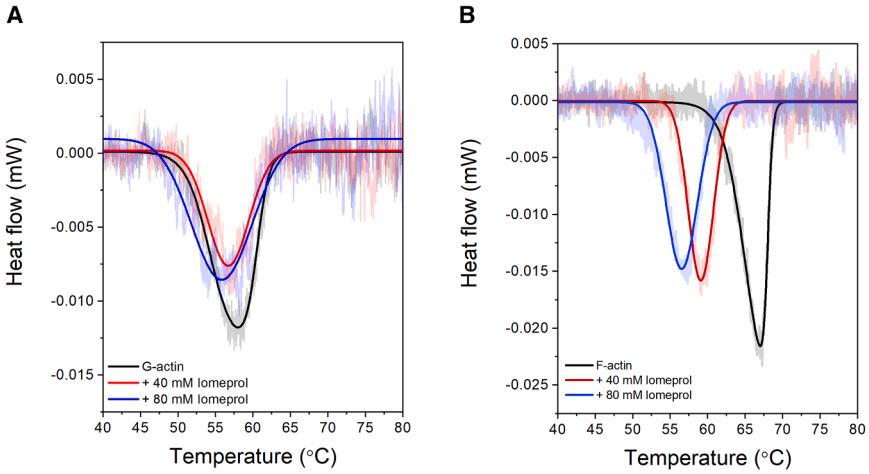

Figure 3. Thermal stability of actin forms. (A) G-actin and (B) F-actin. Control samples are black, and 40 mM and 80 mM treated samples are red and blue, respectively. Data represent mean ± SD ($n = 3$).

Table 2. Thermodynamic characterization of G- and F-actin in the absence and presence of iomeprol (40, 80 mM)

Thermodynamic parameters by DSC		
	T_m (°C)	ΔH (KJ/mol)
G-actin	58.2 ± 0.28	687.5 ± 147.19
+40 mM iomeprol	57.2 ± 0.56	637.2 ± 112.65
+80 mM iomeprol	56.3 ± 0.63	563.3 ± 49.76
F-actin	67.1 ± 0.14	744.7 ± 143.75
+40 mM iomeprol	59.7 ± 0.77	637.9 ± 40.51
+80 mM iomeprol	57.6 ± 1.55	554.1 ± 57.26

Overall, the fluorescence emission-based spectral shift measurements revealed that the mant-ATP affinity for G-actin was considerably decreased by more than 3-fold upon iomeprol treatment. We propose that the binding pocket becomes more surface exposed due to a conformational change, and/or mant-ATP binds ATP-depleted G-actin with weaker affinity than iomeprol. This is consistent with the ITC results, which show that iomeprol binds G-actin with higher affinity (Figure 2; Table 1).

Iomeprol interacts with the ATP binding pocket of actin

The binding mode of iomeprol to G-actin was systematically mapped using the Wrapper step of the Wrap'n'Shake method.[42] The whole surface of G-actin was covered by a monolayer of iomeprol copies (Figure 9). The 1st ranked binding mode corresponding to the most favorable binding energy (−7.36 kcal/mol) was placed close to the ATP binding pocket (number 1 on Figure 10). Two additional binding modes (−3.33 and −2.48 kcal/mol) were identified within 3.5 Å of the ATP molecule (numbers 2 and 3 on Figure 10). Binding modes 2 and 3 cover the entrance to the ATP binding pocket. Binding mode 1 can be considered a strong prerequisite binding mode[60,61] to 2 and 3, which can influence the association/dissociation of ATP from G-actin.

An additional binding mode was found in the cleft formed by subdomains (SD) 1 and 3 of G-actin (Figure 9, SD1/3 binding pocket) according to PDB: 2vyp,[62] 4k41, and 4k43.[63] This binding mode was ranked 15th (−5.97 kcal/mol) and showed a significant overlap with the experimental binding modes of rhizopodin 62 and two analogs of aplyronine C.[63]

DISCUSSION

Contrast agents are indispensable tools in modern diagnostic and interventional radiology, yet their biological impact at the cellular and molecular level remains incompletely understood. Clinical and experimental observations consistently show that iodinated contrast media can impose substantial stress on exposed tissues, particularly within the kidney, where high filtration loads, osmotic effects, and delayed tubular clearance promote both extracellular and intracellular accumulation.[9–11,22] Several studies have demonstrated that contrast agents can reach millimolar to sub-hundred-millimolar concentrations in tubular fluid and within endosomal-lysosomal compartments of epithelial cells, and that local peak concentrations may be even higher during intra-arterial administration.[15–18] Such exposure conditions are known to perturb membrane integrity, alter cell morphology, and interfere with cytoskeletal organization, including actin-dependent processes.[11,22,23]

Given the central role of actin in maintaining cell structure, motility, intracellular transport, and signal transduction,[27–33] even subtle perturbations of actin dynamics may

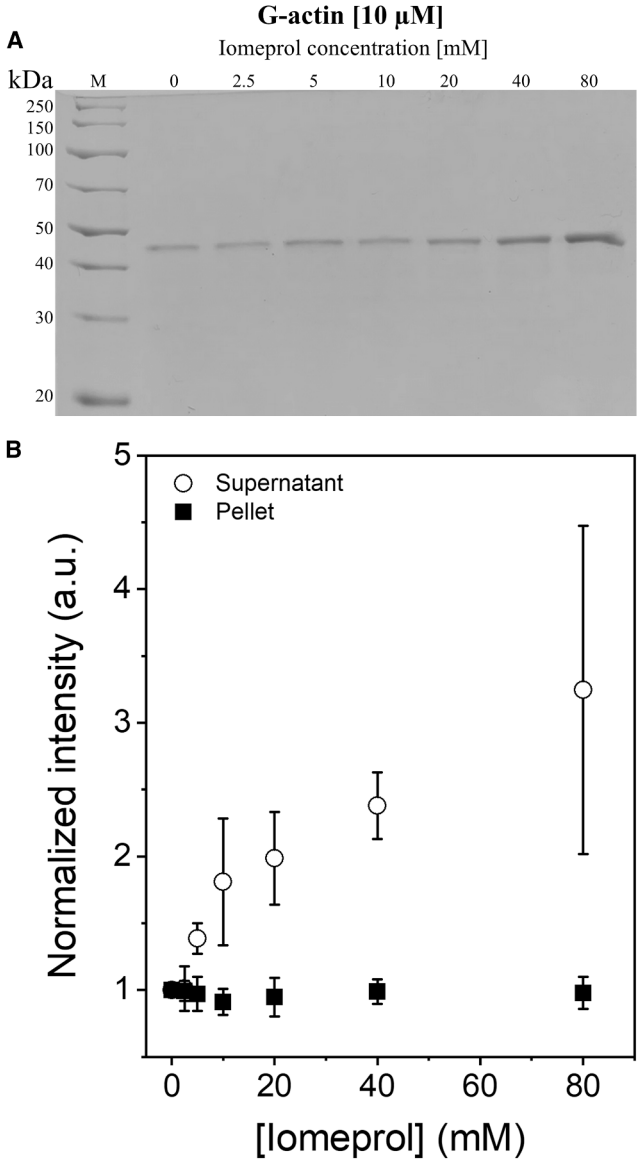

Figure 4. High-speed F-actin co-sedimentation assay. (A) Increasing amount of G-actin in the supernatant after the incubation with increasing concentration (0–80 mM) of iomeprol on PAGE. (B) The normalized intensities of G-actin (supernatant) and F-actin (pellet) were plotted against the increasing concentration of iomeprol. Data represent mean ± SD ($n = 3$).

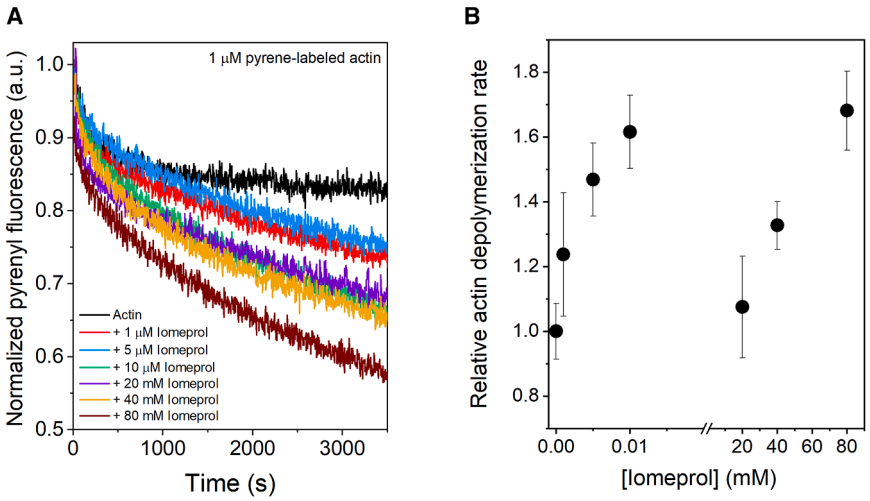

Figure 5. Effect of iomeprol on the depolymerization dynamics of actin. (A) Depolymerization curves of F-actin using 1 μM pyrene-labeled actin. (B) Relative depolymerization rates at 0 μM, 1 μM, 5 μM, 10 μM, and millimolar iomeprol concentrations. Data represent mean ± SD ($n \geq 5$).

contribute to the cellular dysfunction observed after contrast agent exposure. Despite this, the molecular details of how iodinated contrast media interact with actin have remained largely unexplored. In this study, a combination of calorimetric, co-sedimentation, fluorescence spectroscopic, and molecular docking methods was used to investigate the structural and functional properties of actin upon iomeprol administration.

ITC analysis demonstrated a direct and relatively strong interaction between iomeprol and G-actin, with micromolar affinity and a clear 1:1 stoichiometry (Figure 2; Table 1). The modest exothermic enthalpy change and small positive entropy suggest that binding is accompanied by subtle structural rearrangements rather than large-scale unfolding. These thermodynamic features have already hinted that iomeprol may influence the conformational landscape of actin.

This interpretation was confirmed by our DSC measurements, which revealed that iomeprol progressively lowers the thermal stability of both G- and F-actin. In the presence of iomeprol, the conformation of G-actin became more flexible, as indicated by decreased thermodynamic parameters (a 1.9°C drop in T_m and a 124.2-kJ/mol reduction in ΔH) (Figures 3A and 3B; Table 2). The much larger decrease in the melting temperature of F-actin—nearly 10°C at 40 mM—suggests that filament integrity is particularly sensitive to the presence of the contrast agent. Notably, the final T_m of F-actin in the presence of high iomeprol concentrations approached that of monomeric actin, supporting the idea that iomeprol promotes filament disassembly rather than merely destabilizing the folded state.

The co-sedimentation assay further supported this conclusion, as the F:G-actin ratio shifted markedly toward monomers upon iomeprol treatment (Figures 4A and 4B). To complement these equilibrium measurements, we also examined actin dynamics. Depolymerization assays revealed that iomeprol accelerates filament disassembly

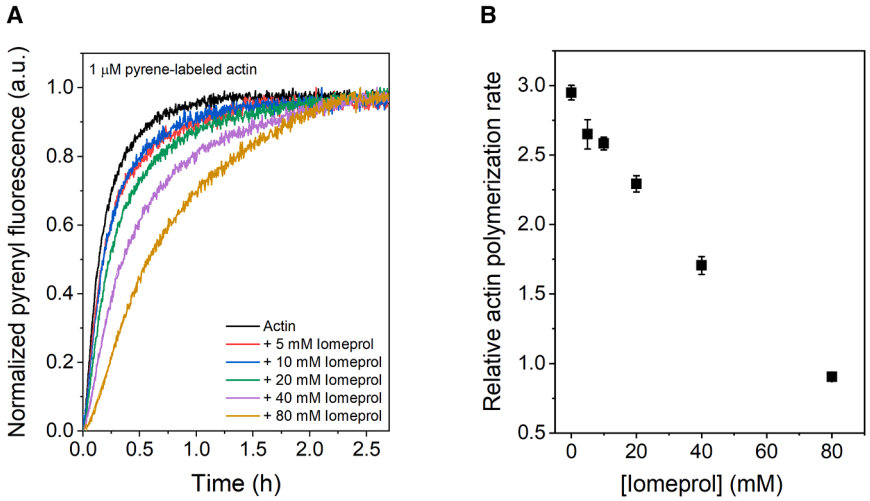

Figure 6. Effect of iomeprol on the polymerization dynamics of actin. (A) Polymerization curves of 1 μM pyrene-labeled actin. (B) Relative polymerization rates at 5 mM, 10 mM, 20 mM, 40 mM, and 80 mM iomeprol concentrations. Data represent mean ± SD ($n = 3$).

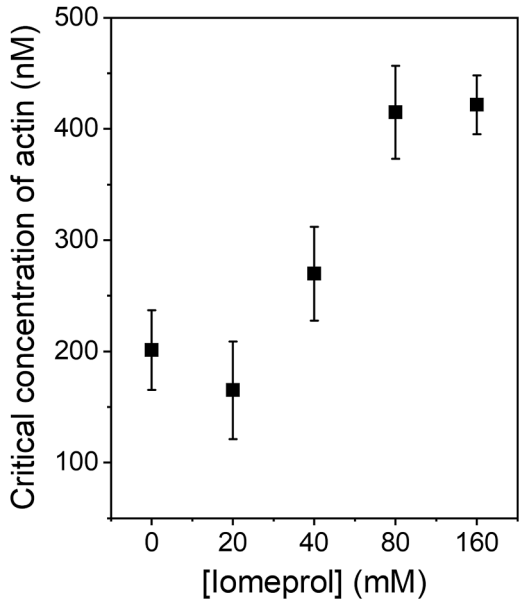

Figure 7. Iomeprol slightly affects the critical concentration of actin. 2-fold increase in critical concentration only at very high iomeprol levels. Data represent mean ± SD ($n = 3$).

in a concentration-dependent manner, with an unexpectedly pronounced effect at micromolar concentrations (1–10 μM), comparable to the effects observed at millimolar levels (40–80 mM). (Figures 5A and 5B). Although our dilution-induced depolymerization assay clearly shows that iomeprol accelerates filament disassembly, the underlying mechanism remains unresolved. Under our experimental conditions, a sequestration-type effect can be excluded, as free G-actin does not influence the kinetics of F-actin depolymerization.[45] The increase in depolymerization rate is also modest compared with the pronounced severing activity of proteins such as cofilin or twinfilin.[44,64] Thus, the observed acceleration may arise from more subtle mechanisms, such as weakened inter-subunit contacts or altered ATP hydrolysis dynamics. Taken together, these observations indicate that iomeprol can modulate filament turnover through multiple mechanisms, although the precise molecular basis remains to be clarified. Polymerization assays showed that the presence of iomeprol inhibits actin assembly, and at the highest concentration the initial polymerization velocity decreased nearly 3-fold relative to the control (Figures 6A and 6B). Despite these pronounced kinetic effects, the critical concentration was only modestly affected, increasing by about 2-fold even at 80 mM (Figure 7), indicating that the thermodynamic equilibrium between G- and F-actin remains largely intact.

The apparent discrepancy between the micromolar affinity measured by ITC and the higher concentrations required to markedly affect filament stability can be reconciled by the coexistence of multiple binding modes. Actin is known to engage small molecules through both high-affinity, site-specific interactions and additional low-affinity, surface-distributed contacts that become relevant only at elevated ligand concentrations.[65–67] Similar dual-mode behavior has been described for several actin-associated proteins, including mDia1 formin, which binds the barbed end with high affinity but associates with filament sides only at higher concentrations.[68] Consistent with this model, our depolymerization measurements show that iomeprol accelerates filament disassembly already at micromolar concentrations—matching the ITC-derived affinity—whereas more pronounced destabilization emerges only at millimolar levels. These observations support a mechanism in which a specific micromolar interaction is complemented by weaker, cumulative contacts that influence filament stability under higher exposure conditions.

Spectroscopic analysis of the nucleotide binding pocket provided additional mechanistic insight. Under control conditions, mant-ATP binding induced a characteristic 16-nm blueshift, reflecting burial of the fluorophore within the native ATP cleft. In contrast, iomeprol markedly reduced this spectral shift (∼7 nm), indicating that the nucleotide pocket becomes more solvent exposed and conformationally flexible (Figures 8C–8F). The corresponding decrease in mant-ATP affinity—more than 3-fold at high iomeprol concentrations—further supports the idea that iomeprol perturbs the architecture of the ATP-binding site. These observations align well with the ITC results, which showed that iomeprol binds G-actin with higher affinity than mant-ATP under the same conditions.

Molecular docking provided a structural rationale for these experimental findings. The highest-ranked binding mode placed iomeprol directly adjacent to the ATP-binding pocket, with two additional poses partially occluding the entrance of the cleft (Figure 10). Such positioning could readily interfere with nucleotide association and dissociation, consistent with the reduced mant-ATP affinity observed experimentally.

A second binding site was identified in the SD1/3 cleft (Figure 9), a region known to interact with actin-binding proteins such as WASP and profilin.[24–26] Binding at this site raises the possibility that iomeprol may also modulate the recruitment or release of regulatory proteins, thereby influencing cytoskeletal organization more broadly.

Taken together, our results suggest that iomeprol destabilizes F-actin primarily by binding to G-actin with micromolar affinity and inducing conformational changes that weaken both filament stability and nucleotide binding. The combined biochemical and computational evidence points to a mechanism in which iomeprol perturbs the structural integrity of the ATP-binding pocket and potentially interferes with protein-protein interactions at the SD1/3 interface. These findings highlight

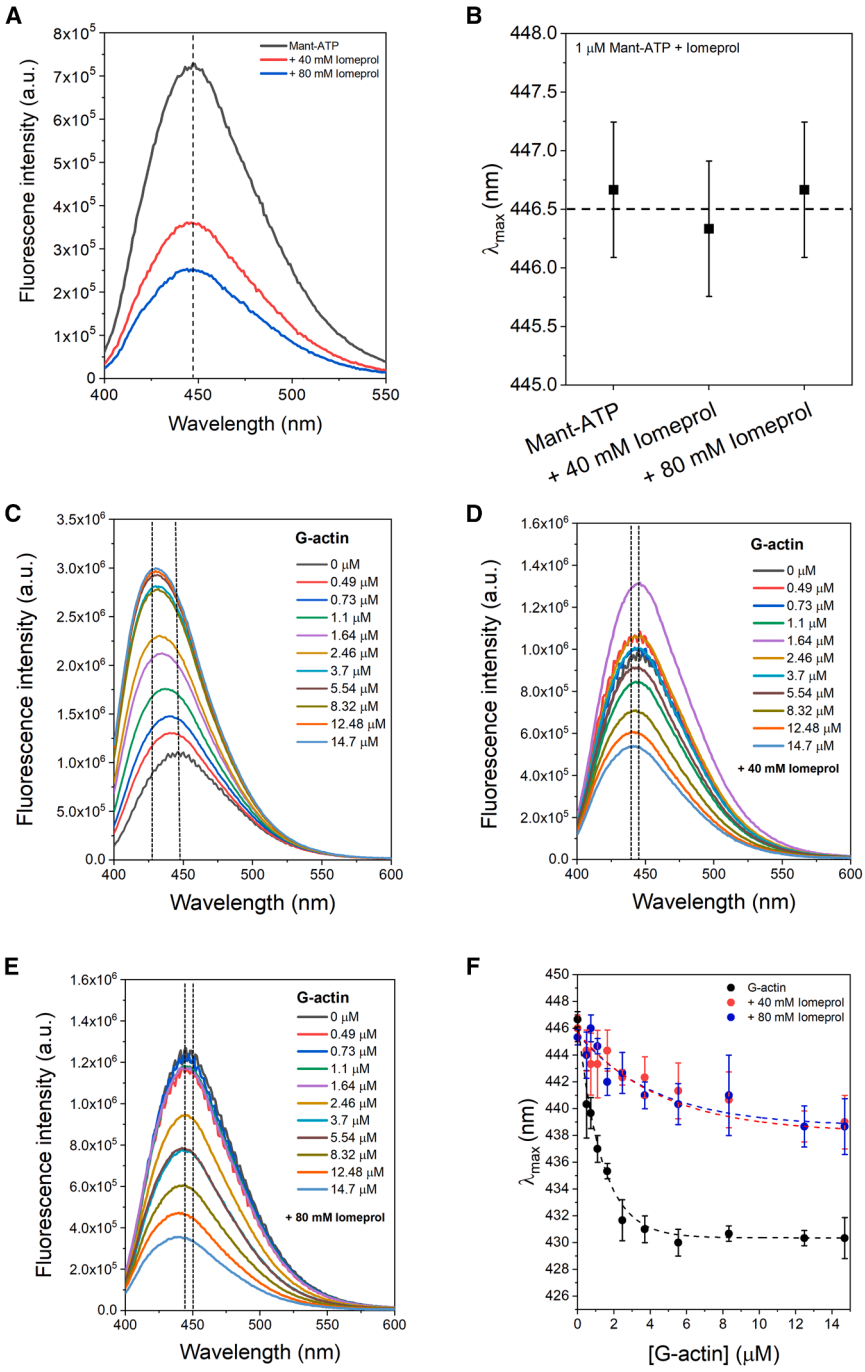

Figure 8. Effect of iomeprol on the spectral emission of the ATP binding pocket of G-actin. Spectral emission of 1 μM Mant-ATP in the absence and presence of iomeprol (40, 80 mM). (A) Emission spectra showed that iomeprol decreases the fluorescence intensity of mant-ATP. (B) Analysis of wavelength maxima of fluorescence emission peaks showed that iomeprol has no effect of the spectral shift of mant-ATP. Fluorescence emission of 1 μM mant-ATP was measured by increasing concentration of ATP-depleted G-actin. Mant-ATP was excited at 365 nm, and the emission was recorded between 400 and 600 nm. The vertical dashed line indicates the spectral shift. The fluorescence emission of mant-ATP in the presence of G-actin (C) showed 16.3-nm blueshift in the wavelength corresponding to the emission maximum from 446.6 to 430.3 nm, while (D) fluorescence emission of mant-ATP in the presence 40 mM iomeprol resulted in a less significant blueshift of 7 nm from 446 to 439 nm. Moreover, (E) fluorescence emission of mant-ATP in the presence of 80 mM iomeprol revealed a similarly low blueshift of 6.7 nm from 446 to 438.7 nm. (F) Maximum wavelength (λ_{max}) of mant-ATP fluorescence emission plotted as a function of G-actin concentration showing spectral shift and indicates possible conformational change of the ATP binding pocket. Data represent mean ± SD ($n = 3$).

the possibility that iodinated contrast agents may exert previously unrecognized effects on ATP-dependent functions of actin and on the regulation of the actin cytoskeleton.[69,70]

DATA AVAILABILITY

Measurement data and molecular modeling results supporting this study have been deposited in Mendeley Data under the accession link https://doi.org/10.17632/f24bk29zmy.2 and will be publicly available upon publication of the article.

ACKNOWLEDGMENTS

This paper was supported by the University of Pécs, Medical School, Dr. Romhányi György Fellowship for Young Scientist (ÁOK-IK) (E.T.) and Medical School at University of Pécs KA-2024-10 (Z.U.) as well as by the János Bolyai Research Scholarship of the Hungarian Academy of Sciences (B.Z.Zs.). The work was supported by the National Research,

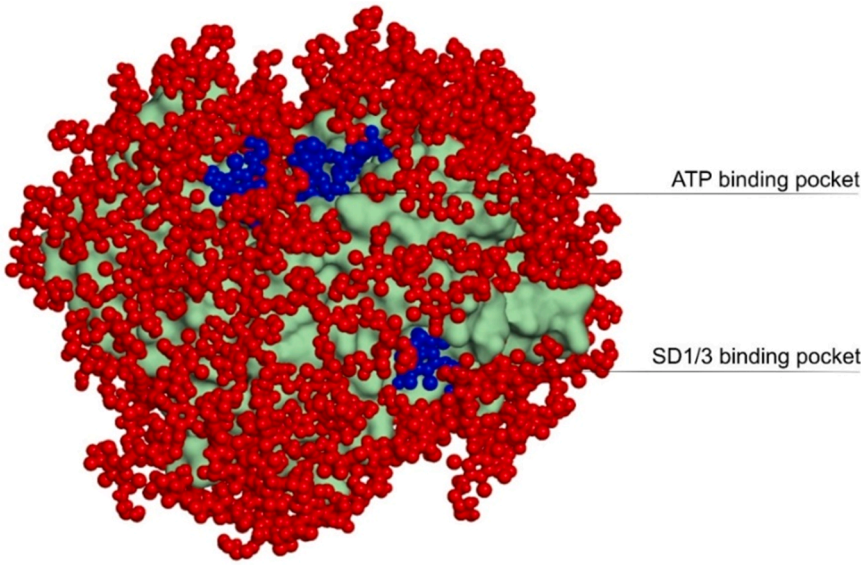

Figure 9. G-actin (green surface) covered with a monolayer of the copies of iomeprol (red spheres). The iomeprol copies bound to the ATP or the subdomain 1/3 (SD1/3) binding pockets are highlighted with blue.

Development and Innovation Office, Hungary (PharmaLab, RRF-2.3.1-21-2022-00015) (Cs.H.). We acknowledge the Digital Government Development and Project Management Ltd. for awarding us access to the Komondor HPC facility based in Hungary. We are grateful for financial support from the Hungarian National Research and Innovation Office in the frame of the 2024-1.2.3-HU-RIZONT-2024-00063 grant (A.L.).

AUTHOR CONTRIBUTIONS

Z.U. conceived the study. E.T. contributed to the conception of the study. E.T., V.T.-K., K.U.-P., Z.Cs., B.Z.Zs., Cs.H., B.B., and Z.U. designed and performed experiments. E.T., V.T.-K., K.U.-P., Z.Cs., B.Z.Zs., Cs.H., B.B., Z.U., and S.K.-M. were involved in the data analysis. E.T. and U.Z. wrote the first draft of the manuscript. E.T., V.T.-K., K.U.-P., Z.Cs., B.Z.Zs., Cs.H., B.B., A.L., G.H., and Z.U. reviewed the manuscript. All authors were responsible for the final version of the manuscript.

DECLARATION OF INTERESTS

The authors have no conflicts of interest to declare that are relevant to the content of this article.

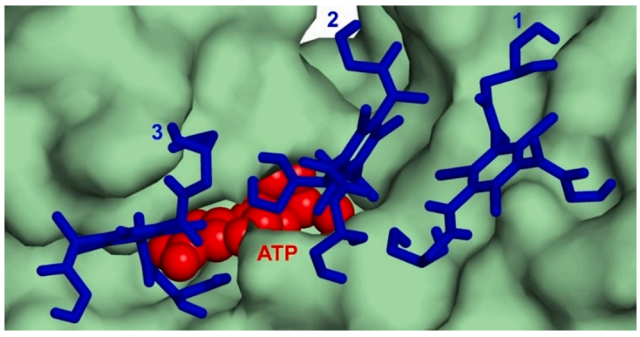

Figure 10. The close-up of the ATP binding pocket. G-actin is shown as a green surface, iomeprol copies are shown as blue sticks and numbered 1–3, and ATP is shown as red spheres.

REFERENCES

1. Haschek, E. ,L. O. 1896. A contribution to the practical use of photography according to Roentgen. *Wien Chir Wochenschr.* 9:63.
2. Osborne, E. D., C. G. Sutherland, …, L. G. Rowntree. 1923. Roentgenography of urinary tract during excretion of sodium iodid. *J. Am. Med. Assoc.* 80:368–373. https://doi.org/10.1001/jama.1923.02640330004002.
3. Lusic, H., and M. W. Grinstaff. 2013. X-ray-computed tomography contrast agents. *Chem. Rev.* 113:1641–1666. https://doi.org/10.1021/cr200358s.
4. Hao, D., T. Ai, …, M. Tweedle. 2012. MRI contrast agents: Basic chemistry and safety. *J. Magn. Reson. Imag.* 36:1060–1071. https://doi.org/10.1002/jmri.23725.
5. Khairnar, S., N. More, …, G. Kapusetti. 2019. Advances in Contrast Agents for Contrast-Enhanced Magnetic Resonance Imaging. *J. Med. Imag. Radiat. Sci.* 50:575–589. https://doi.org/10.1016/j.jmir.2019.09.006.
6. Krause, W. 1999. Delivery of diagnostic agents in computed tomography. *Adv. Drug Deliv. Rev.* 37:159–173. https://doi.org/10.1016/S0169-409X(98)00105-7.
7. Eldem, F. G., and B. Peynircioğlu. 2021. Contrast Agents in Vascular Interventional Radiology. *In* Medical Imaging Contrast Agents: A Clinical Manual. S. M. Erturk, P. R. Ros, and …, S. Saylisoyeds Springer International Publishing, pp. 289–304.
8. Brogan, W. C., L. D. Hillis, and R. A. Lange. 1991. Contrast agents for cardiac catheterization: Conceptions and misconceptions. *Am. Heart J.* 122:1129–1135. https://doi.org/10.1016/0002-8703(91)90481-V.
9. Po-Tsang, L., C. Kang-Ju, …, C. Hsiao-Min. 2007. Renal Protection for Coronary Angiography in Advanced Renal Failure Patients by Prophylactic Hemodialysis. *J. Am. Coll. Cardiol.* 50:1015–1020. https://doi.org/10.1016/j.jacc.2007.05.033.
10. Kusirisin, P., S. C. Chattipakorn, and N. Chattipakorn. 2020. Contrast-induced nephropathy and oxidative stress: mechanistic insights for better interventional approaches. *J. Transl. Med.* 18:400. https://doi.org/10.1186/s12967-020-02574-8.
11. Li, Y., and J. Wang. 2024. Contrast-induced acute kidney injury: a review of definition, pathogenesis, risk factors, prevention and treatment. *BMC Nephrol.* 25:140. https://doi.org/10.1186/s12882-024-03570-6.
12. Franke, R. P., R. Fuhrmann, …, F. Jung. 2011. Influence of radiographic contrast media (Iodixanol und Iomeprol) on the morphology of human arterial and venous endothelial cells on extracellular matrix

in vitro. *Clin. Hemorheol. Microcirc.* 48:41–56. https://doi.org/10.3233/CH-2011-1404.

13. Rosati, G. 1994. Clinical utility and safety profile of iomeprol. *Eur. J. Radiol.* 18:S120–S124.
14. Lorusso, V., P. Taroni, …, A. Spinazzi. 2001. Pharmacokinetics and Safety of Iomeprol in Healthy Volunteers and in Patients with Renal Impairment or End-Stage Renal Disease Requiring Hemodialysis. *Investig. Radiol.* 36:309–316. https://doi.org/10.1097/00004424-200106000-00002.
15. Persson, P. B., P. Hansell, and P. Liss. 2005. Pathophysiology of contrast medium-induced nephropathy. *Kidney Int.* 68:14–22.
16. Heinrich, M. C., M. K. Kuhlmann, …, M. Uder. 2007. Cytotoxicity of iodinated and gadolinium-based contrast agents in renal tubular cells at angiographic concentrations: In vitro study. *Radiology.* 242:425–434. https://doi.org/10.1148/radiol.2422060245.
17. Sendeski, M. M. 2011. Pathophysiology of renal tissue damage by iodinated contrast media. *Clin. Exp. Pharmacol. Physiol.* 38:292–299. https://doi.org/10.1111/j.1440-1681.2011.05503.x.
18. Liu, Z. Z., K. Schmerbach, …, M. M. Sendeski. 2014. Iodinated contrast media cause direct tubular cell damage, leading to oxidative stress, low nitric oxide, and impairment of tubuloglomerular feedback. *Am. J. Physiol. Ren. Physiol.* 306:864–872. https://doi.org/10.1152/ajprenal.00302.2013.-Iodinated.
19. Rengo, M., A. Dharampal, …, K. Nieman. 2019. Impact of iodine concentration and iodine delivery rate on contrast enhancement in coronary CT angiography: a randomized multicenter trial (CT-CON). *Eur. Radiol.* 29:6109–6118. https://doi.org/10.1007/s00330-019-06196-7/Published.
20. Silvennoinen, H. M., L. M. Hamberg, …, G. J. Hunter. 2007. Increasing contrast agent concentration improves enhancement in first-pass CT perfusion. *Am. J. Neuroradiol.* 28:1299–1303. https://doi.org/10.3174/ajnr.A0574.
21. Du, Y., Y. N. Wang, …, X. Liu. 2023. A comparison of the use of contrast media with different iodine concentrations for enhanced computed tomography. *Front. Physiol.* 14:1141135. https://doi.org/10.3389/fphys.2023.1141135.
22. Mrowietz, C., R. P. Franke, and F. Jung. 2012. Influence of different radiographic contrast media on the echinocyte formation of human erythrocytes. *Clin. Hemorheol. Microcirc.* 50:35–47. https://doi.org/10.3233/CH-2011-1441.
23. Franke, R. P., T. Scharnweber, …, F. Jung. 2013. Distribution of actin of the human erythrocyte membrane cytoskeleton after interaction with radiographic contrast media. *Clin. Hemorheol. Microcirc.* 55:481–490. https://doi.org/10.3233/CH-131789.
24. Dominguez, R. 2004. Actin-binding proteins – a unifying hypothesis. *Trends Biochem. Sci.* 29:572–578. https://doi.org/10.1016/J.TIBS.2004.09.004.
25. Chereau, D., F. Kerff, …, R. Dominguez. 2005. Actin-bound structures of Wiskott-Aldrich syndrome protein (WASP)-homology domain 2 and the implications for filament assembly. *Proc. Natl. Acad. Sci. USA.* 102:16644–16649.
26. Schutt, C. E., J. C. Myslik, …, U. Lindberg. 1993. The structure of crystalline profilin–β-actin. *Nature.* 365:810–816. https://doi.org/10.1038/365810a0.
27. Chalut, K. J., and E. K. Paluch. 2016. The Actin Cortex: A Bridge between Cell Shape and Function. *Dev. Cell.* 38:571–573. https://doi.org/10.1016/J.DEVCEL.2016.09.011.
28. Wu, Y., and S. X. Sun. 2023. Mechanics of cell-cell junctions. *Biophys. J.* 122:3354–3368. https://doi.org/10.1016/J.BPJ.2023.07.011.
29. Pollard, T. D., and G. G. Borisy. 2003. Cellular Motility Driven by Assembly and Disassembly of Actin Filaments. *Cell.* 112:453–465. https://doi.org/10.1016/S0092-8674(03)00120-X.
30. Narita, A., J. Mueller, …, Y. Maéda. 2012. Direct Determination of Actin Polarity in the Cell. *J. Mol. Biol.* 419:359–368. https://doi.org/10.1016/J.JMB.2012.03.015.
31. Gibieža, P., and V. Petrikaitė. 2021. The regulation of actin dynamics during cell division and malignancy. *Am. J. Cancer Res.* 11:4050–4069.
32. Schuh, M. 2011. An actin-dependent mechanism for long-range vesicle transport. *Nat. Cell Biol.* 13:1431–1436. https://doi.org/10.1038/ncb2353.
33. Carpenter, C. L. 2000. Actin cytoskeleton and cell signaling. *Crit. Care Med.* 28:N94–N99. https://doi.org/10.1097/00003246-200004001-00011.
34. Ujfalusi, Z., E. Telek, …, G. Hild. 2022. The effect of Iodixanol on the thermodynamic properties of blood components. *Thermochim. Acta.* 710:179165. https://doi.org/10.1016/j.tca.2022.179165.
35. Telek, E., Z. Ujfalusi, …, G. Hild. 2023. Deconvolution Analysis of the Non-Ionic Iomeprol, Iobitridol and Iodixanol Contrast Media-Treated Human Whole Blood Thermograms: A Comparative Study. *Diagnostics.* 13:2523. https://doi.org/10.3390/diagnostics13152523.
36. Spudich, J. A., and S. Watt. 1971. The Regulation of Rabbit Skeletal Muscle Contraction. *J. Biol. Chem.* 246:4866–4871.
37. 2024. Schrödinger Release 2024-1. Maestro, Schrödinger, LLC.
38. Gasteiger, J., and M. Marsili. 1980. Iterative partial equalization of orbital electronegativity—a rapid access to atomic charges. *Tetrahedron.* 36:3219–3228. https://doi.org/10.1016/0040-4020(80)80168-2.
39. Morris, G. M., R. Huey, …, A. J. Olson. 2009. AutoDock4 and AutoDockTools4: Automated docking with selective receptor flexibility. *J. Comput. Chem.* 30:2785–2791. https://doi.org/10.1002/jcc.21256.
40. Wang, H., R. C. Robinson, and L. D. Burtnick. 2010. The structure of native G-actin. *Cytoskeleton.* 67:456–465. https://doi.org/10.1002/cm.20458.
41. Waterhouse, A., M. Bertoni, …, T. Schwede. 2018. SWISS-MODEL: homology modelling of protein structures and complexes. *Nucleic Acids Res.* 46:W296–W303. https://doi.org/10.1093/nar/gky427.
42. Bálint, M., N. Jeszenői, …, C. Hetényi. 2017. Systematic exploration of multiple drug binding sites. *J. Cheminform.* 9:65. https://doi.org/10.1186/s13321-017-0255-6.
43. Payrits, M., B. Z. Zsidó, …, É. Szőke. 2024. Lipid raft disruption inhibits the activation of Transient Receptor Potential Vanilloid 1, but not TRP Melastatin 3 and the voltage-gated L-type calcium channels in sensory neurons. *Front. Cell Dev. Biol.* 29:1452306. https://doi.org/10.3389/fcell.2024.1452306.
44. Takács-Kollár, V., D. Lőrinczy, …, G. Hild. 2016. Spectroscopic characterization of the effect of mouse twinfilin-1 on actin filaments at different pH values. *J. Photochem. Photobiol. B Biol.* 164:276–282. https://doi.org/10.1016/J.JPHOTOBIOL.2016.09.044.
45. Cano, M. L., D. A. Lauffenburger, and S. H. Zigmond. 1991. Kinetic Analysis of F-actin Depolymerization in Pblymorphonuclear Leukocyte Lysates Indicates That Chemoattractant Stimulation Increases Actin Filament Number without Altering the Filament Length Distribution. *J. Cell Biol.* 115:677–687. https://doi.org/10.1083/jcb.115.3.677.
46. Greve, J. N., A. Marquardt, …, D. J. Manstein. 2024. The non-muscle actinopathy-associated mutation E334Q in cytoskeletal γ-actin perturbs interaction of actin filaments with myosin and ADF/cofilin family proteins. *eLife.* 12:RP93013. https://doi.org/10.7554/elife.93013.
47. Lima Cavalcanti, I. D., F. H. Xavier Junior, …, M. C. d. B. Lira Nogueira. 2023. Isothermal titration calorimetry (ITC) as a promising tool in pharmaceutical nanotechnology. *Int. J. Pharm.* 641:123063. https://doi.org/10.1016/j.ijpharm.2023.123063.
48. Kónya, Z., I. Tamás, …, F. Erdődi. 2023. Phosphorylated Peptide Derived from the Myosin Phosphatase Target Subunit Is a Novel Inhibitor of Protein Phosphatase-1. *Int. J. Mol. Sci.* 24:4789. https://doi.org/10.3390/ijms24054789.
49. Garbett, N. C., and G. N. Brock. 2016. Differential scanning calorimetry as a complementary diagnostic tool for the evaluation of biological samples. *Biochim. Biophys. Acta.* 1860:981–989. https://doi.org/10.1016/j.bbagen.2015.10.004.

50. Takács-Kollár, V., M. Nyitrai, …, G. Hild. 2018. Calorimetric characterisation of the toxofilin–G-actin complex. *J. Therm. Anal. Calorim.* 131:1307–1311. https://doi.org/10.1007/s10973-017-6698-1.

51. Pivovarova, A. V., N. A. Chebotareva, …, D. I. Levitsky. 2013. Effects of actin-binding proteins on the thermal stability of monomeric actin. *Biochemistry.* 52:152–160. https://doi.org/10.1021/bi3012884.

52. Kardos, R., E. Nevalainen, …, G. Hild. 2013. The effect of ADF/cofilin and profilin on the dynamics of monomeric actin. *Biochim. Biophys. Acta.* 1834:2010–2019. https://doi.org/10.1016/j.bbapap.2013.06.006.

53. Telek, E., Z. Ujfalusi, …, G. Hild. 2022. A Possible Way to Relate the Effects of SARS-CoV-2-Induced Changes in Transferrin to Severe COVID-19-Associated Diseases. *Int. J. Mol. Sci.* 23:6189. https://doi.org/10.3390/ijms23116189.

54. Ujfalusi, Z., A. Vig, …, M. Nyitrai. 2009. Effect of Tropomyosin on Formin-Bound Actin Filaments. *Biophys. J.* 96:162–168. https://doi.org/10.1529/biophysj.108.138420.

55. Bagshaw, C. 2001. ATP analogues at a glance. *J. Cell Sci.* 114:459–460. https://doi.org/10.1242/jcs.114.3.459.

56. Nyitrai, M., A. G. Szent-Györgyi, and M. A. Geeves. 2002. A kinetic model of the co-operative binding of calcium and ADP to scallop (Argopecten irradians) heavy meromyosin. *Biochem. J.* 365:19–30. https://doi.org/10.1042/bj20020099.

57. Patel, J. T., H. R. Belsham, …, C. T. Friel. 2014. Use of Stopped-Flow Fluorescence and Labeled Nucleotides to Analyze the ATP Turnover Cycle of Kinesins. *J. Vis. Exp.* 17:e52142. https://doi.org/10.3791/52142.

58. Raics, K., K. Pirisi, …, A. Lukacs. 2023. Photocycle alteration and increased enzymatic activity in genetically modified photoactivated adenylate cyclase OaPAC. *J. Biol. Chem.* 299:105056. https://doi.org/10.1016/j.jbc.2023.105056.

59. Ujfalusi-Pozsonyi, K., E. Bódis, …, A. Lukács. 2024. ATP-dependent conformational dynamics in a photoactivated adenylate cyclase revealed by fluorescence spectroscopy and small-angle X-ray scattering. *Commun. Biol.* 7:1–15. https://doi.org/10.1038/s42003-024-05842-1.

60. Zsidó, B. Z., R. Börzsei, …, C. Hetényi. 2021. Prerequisite binding modes determine the dynamics of action of covalent agonists of ion channel trpa1. *Pharmaceuticals.* 14:988. https://doi.org/10.3390/ph14100988.

61. Bálint, M., B. Z. Zsidó, …, C. Hetényi. 2022. Binding Networks Identify Targetable Protein Pockets for Mechanism-Based Drug Design. *Int. J. Mol. Sci.* 23:7313. https://doi.org/10.3390/ijms23137313.

62. Hagelueken, G., S. C. Albrecht, …, W.-D. Schubert. 2009. The Absolute Configuration of Rhizopodin and Its Inhibition of Actin Polymerization by Dimerization. *Angew Chem. Int. Ed.* 48:595–598. https://doi.org/10.1002/anie.200802915.

63. Pereira, J. H., C. Petchprayoon, …, G. Marriott. 2014. Structural and Biochemical Studies of Actin in Complex with Synthetic Macrolide Tail Analogues. *ChemMedChem.* 9:2286–2293. https://doi.org/10.1002/cmdc.201402150.

64. Normoyle, K. P. M., and W. M. Brieher. 2012. Cyclase-associated protein (CAP) acts directly on F-actin to accelerate cofilin-mediated actin severing across the range of physiological pH. *J. Biol. Chem.* 287:35722–35732. https://doi.org/10.1074/jbc.M112.396051.

65. Yarmola, E. G., T. Somasundaram, …, M. R. Bubb. 2000. Actin-latrunculin a structure and function: Differential modulation of actin-binding protein function by latrunculin A. *J. Biol. Chem.* 275:28120–28127. https://doi.org/10.1074/jbc.M004253200.

66. Cooper, J. A. 1987. Mini-Review Effects of Cytochalasin and Phalloidin on Actin. *J. Cell Biol.* 105:1473–1478. https://doi.org/10.1083/jcb.105.4.1473.

67. Oda, T., M. Iwasa, …, A. Narita. 2009. The nature of the globular- to fibrous-actin transition. *Nature.* 457:441–445. https://doi.org/10.1038/nature07685.

68. Bugyi, B., G. Papp, …, M. Nyitrai. 2006. Formins regulate actin filament flexibility through long range allosteric interactions. *J. Biol. Chem.* 281:10727–10736. https://doi.org/10.1074/jbc.M510252200.

69. Zigmond, S. H. 2000. How Wasp Regulates Actin Polymerization. *J. Cell Biol.* 150:F117–F120. https://doi.org/10.1083/jcb.150.6.F117.

70. Pinto-Costa, R., and M. M. Sousa. 2020. Profilin as a dual regulator of actin and microtubule dynamics. *Cytoskeleton.* 77:76–83. https://doi.org/10.1002/cm.21586.